PAPER

Check for updates

One-pot mechanochemical ball milling synthesis of the MnO$_x$ nanostructures as efficient catalysts for CO$_2$ hydrogenation reactions†

Altantuya Ochirkhuyag, [ID] [a] András Sápi, [ID] *[ab] Ákos Szamosvölgyi,[a] Gábor Kozma,[a] Ákos Kukovecz[ac] and Zoltán Kónya [ID] [ac]

Here, we report on a one-pot mechanochemical ball milling synthesis of manganese oxide nanostructures synthesized at different milling speeds. The as-synthesized pure oxides and metal (Pt and Cu) doped oxides were tested in the hydrogenation of CO$_2$ in the gas phase. Our study demonstrates the successful synthesis of the manganese oxide nanoparticles *via* mechano–chemical synthesis. We discovered that the milling speed could tune the crystal structure and the oxidation state of the manganese, which plays an essential role in the CO$_2$ hydrogenation evidenced by *ex situ* XRD and XPS studies. The pure MnO$_x$ milled at 600 rpm showed high catalytic activity ($\sim$20 000 nmol g^{-1} s^{-1}) at 823 K, which can be attributed to the presence of Mn(II) besides Mn(III) and Mn(IV) on the surface under the reaction conditions. This study illustrates that the milling method is a cost-effective, simple way for the production of both pure, Pt-doped and Cu-loaded manganese nanocatalysts for heterogeneous catalytic reactions. Thus, we studied the Pt incorporation effect for the catalytic activity of MnO$_x$ using different Pt loading methods such as one-pot milling, wet impregnation and size-controlled 5 nm Pt loading *via* an ultrasonication-assisted method.

1. Introduction

Some of the biggest concerns of our modern world are environmental pollution, global warming, extreme weather changes caused by the emission of CO$_2$ and depleting conventional energy sources such as fossil fuels. CO$_2$ transformation towards valuable fuels (*e.g.*, CH$_4$, CO, methanol, C$_{2+}$, *etc.*) is a promising candidate in next-generation energy source production, as well as in the reduction of environmental stress.[1,2] New generation plants for CO$_2$ hydrogenation are producing methanol with a high conversion rate, even at a production rate of 5500 tons per year.[3] New methods are available to produce C$_{5+}$ hydrocarbons, however, their industrial production has not yet started.[4,5] The reverse water–gas shift reaction (RWGS–CO$_2$ + H$_2$ = CO + H$_2$O) and the subsequent reaction, so-called Sabatier (methanation) reaction (CO$_2$ + 4H$_2$ = CH$_4$ + 2H$_2$O) are also industrial ways to convert CO$_2$ into valuable fuels. In several countries, power-to-gas (PtG) technology is used for the storage of electrical power into chemical energy, where CH$_4$ is the fuel and the product of the CO$_2$ hydrogenation reaction.[6]

In recent years, the most studied CO$_2$ hydrogenation catalysts are nickel-based (Ni/ZrO$_2$, Ni–Ga, and Ni/CeO$_2$);[7–10] typically, they have several shortcomings, such as their pyrophoricity, low stability, and fast deactivation.[11] Manganese-based materials, on the other hand, are not widely researched; however, they can be cost-effective alternatives for catalyzing the CO$_2$ hydrogenation process.[12,13] The fifth most abundant metal in the earth's crust is manganese and it occurs with various types of mineral forms in nature.[14,15] The manganese-based compounds are crucial components in supercapacitors, electrochemical cells for rechargeable batteries, the degradation of organic dyes, removal of the heavy metals from the polluted water, water oxidation and soot combustion.[16–22] Typically, catalytic activity for CO$_2$ reduction and hydrogenation can be improved by a tiny amount of doping or tuning by promoting noble metals such as platinum.[23] Non-noble metal-doped catalysts such as copper[24] also exist for CO$_2$ hydrogenation, but they are barely mentioned in the literature.

Different types of manganese oxides can be synthesized at a laboratory scale, but the industrial level production of MnO$_x$, with stable oxidation states and structure, relies on hydrothermal, solvothermal reactions, heating, and electrochemical deposition.[25–28] The mechanochemical synthesis is suitable for the large-scale production of a variety of nanomaterials and catalysts,[29–33] but a

a University of Szeged, Interdisciplinary Excellence Centre, Department of Applied and Environmental Chemistry, H-6720, Rerrich Béla tér 1, Szeged, Hungary. E-mail: sapia@chem.u-szeged.hu

b Institute of Environmental and Technological Sciences, University of Szeged, H-6720, Szeged, Hungary

c MTA-SZTE Reaction Kinetics and Surface Chemistry Research Group, University of Szeged, H-6720 Szeged, Rerrich Béla tér 1, Szeged, Hungary

† Electronic supplementary information (ESI) available: Details of the characterization data. See DOI: 10.1039/d0cp01855d

This journal is © the Owner Societies 2020

Phys. Chem. Chem. Phys., 2020, **22**, 13999–14012 | 13999

few reports in the literature have described the synthesis of manganese oxides *via* this process.[34–37] The mechanochemical synthesis can be tuned by many parameters such as the milling rotation speed, the milling time, the solvent-template, the weight ratios of the milling mixtures and milling balls, the milling atmosphere, the type of mills, and additional treatments such as sonication or heat treatments as well.[38–43] The conventional dry milling method has significant drawbacks such as wider size distribution of materials, material loss, and friction. Nowadays, wet milling methods are more often used for nanomaterial synthesis.[44–47] Besides, we can map the milling energy. This is important when the different catalytic activities of each sample is compared as it allows the preparation of a more favourable catalyst.

Here, we report on a simple and cost-effective, mechanochemical, one-pot synthesis method to produce pure as well as Pt-loaded or Cu-loaded manganese oxide nanostructures. Our team is the first to report the adjusted conditions for the synthesis of manganese oxides with this method, such as the particular molar ratio of the precursors, water-assisted grinding (wet grinding), milling time and milling rotation speed. One-pot synthesis can be simplify the additional metal doping process into manganese-oxides as using one-step for the whole synthesis. The MnO_x nanostructures were characterized by BET, XRD, Raman, TG, DSC, SEM-EDX, TEM as well as *ex situ* XPS and XRD to explore the effect of pore structure, specific surface area as well as the oxidation states of the manganese in the catalytic reduction of CO_2 with hydrogen. We found that the catalytic activity of the manganese-oxides could be tuned by the milling speed as well as the one-pot addition of active metals where *ex situ* XPS and XRD showed the crucial role of the oxidation states of the manganese under the reaction conditions.

2 Methods

2.1 Materials

Manganese(II) chloride tetrahydrate ($MnCl_2 \cdot 4H_2O$), potassium permanganate ($KMnO_4$), platinum(IV) chloride ($H_2PtCl_6 \cdot H_2O$), copper(II) chloride ($CuCl_2$), sodium hydroxide (NaOH), platinum(II) acetylacetonate ($C_{10}H_{16}O_4Pt$), polyvinylpyrrolidone (PVP, M_W = 40 000) and ethylene-glycol ($CH_2OH)_2$ were used for the synthesis of the manganese-oxide nanostructures. All chemicals and reagents were of analytical grade, purchased from Sigma Aldrich and used without further purification. Ultrapure water was used for all synthesis and washing.

2.2 The synthetic procedure of the manganese-oxide-based catalysts

All the synthetic procedures are described in Table 1. First, we synthesized pure MnO_x (M200, M450, M600) samples by the mechanochemical method with different milling speeds as categorized ball milling (pure samples). Furthermore, we synthesized metal-doped MnO_x samples: M200(Cu-milled), M450(Cu-milled), M600(Cu-milled), M200(Pt-milled), M450-(Pt-milled), and M600(Pt-milled) using the mechanochemical method as categorized ball milling (metal-doped) (Table 1).

To study the effect of platinum incorporation, we prepared additionally Pt-loaded M600 samples using two other methods: Pt loading from H_2PtCl_6 by wet impregnation (M600-Pt-impregnated) and size-controlled 5 nm Pt nanoparticles loading by sonication (M600-5 nm Pt-sonicated) (Table 1).

2.3 Characterization methods

A Rigaku Miniflex II powder X-ray diffractometer using a Cu Kα radiation source (λ = 0.15418 nm) operating at 30 kV and 15 mA at room temperature and a scanning rate of 0.5 degree min^{-1} in the 10–65° 2θ range was used for crystal structure characterization. A high-resolution Transmission Electron Microscope HR-TEM (FEI TECNAI G^2 20 X-TWIN) operated at an accelerating voltage of 200 kV and a Scanning Electron Microscope (Hitachi S-4700 Type II instrument (30 kV accelerating voltage) integrated with EDS) were used to perform morphological and compositional studies.

The thermal behaviour of the samples was investigated *via* Thermogravimetry (TA Instruments Q500 TGA). The instrument worked from RT – 750 °C under both an air and nitrogen atmosphere, where the heating rate was 5 °C min^{-1}. All the samples weighed between 10–20 mg and were placed into high-purity alpha platinum crucibles. Differential scanning calorimetric analysis was performed using Q20 (TA Instruments) at RT – 600 °C under a constant airflow and the heating–cooling rate was 5 °C min^{-1}.

The Raman spectra were collected using a SENTERRA Raman microscope (Bruker Optics, Inc.) at 532 nm with a 1s integration time (with three repetitions) at a resolution of 4 cm^{-1} and interferometer resolution of 0.5 cm^{-1}. The specific surface area and pore radius were measured using a 3H-2000 BET-A surface area analyzer.

For the analysis of the oxidation states of the manganese in the catalysts, XPS spectra were collected using a SPECS XPS instrument equipped with an XR-50 dual anode X-ray source and a PHOIBOS 150 energy analyzer. All spectra were acquired with a Al Kα radiation source operated at 150 W (14 kV). Survey spectra were collected with a step size of 1 eV and 40 eV pass energy, collecting 1 sweep for each sample. High-resolution spectra of Mn 2p, C 1s, O 1s and Pt 4f regions (latter three not shown) were acquired with 20 eV pass energy and step sizes of 0.1 eV. The Mn 2p regions were fitted with multiplet states taken into consideration, where the method was earlier described by Ilton *et al.*[49] When resolving spectra of mixed oxides of Mn(II), Mn(III) and Mn(IV) data from pure oxides could be used as starting parameters. These parameters include peak positions in binding energies, intensity ratios and FWHM values. Due to the complicated nature of this method, the Mn $2p_{1/2}$ regions were not used for the evaluation. A pre-peak at lower binding energies ($\sim$640 eV) was added, which corresponds to lattice defects.

2.4 Catalytic CO_2 activation reaction over manganese-oxide catalysts

Pretreatment. Before the catalytic experiments, the catalysts were oxidized in an O_2 atmosphere at 300 °C for 30 min to remove any surface contaminants, as well as the PVP capping agent, then they were reduced in H_2 at 300 °C for 60 min.

14000 | *Phys. Chem. Chem. Phys.*, 2020, **22**, 13999–14012

This journal is © the Owner Societies 2020

Table 1 The synthetic procedure of the manganese-oxide-based catalysts

Method	Synthetic procedure	Sample name (code)
Ball milling (pure samples)	$MnCl_2 \cdot 4H_2O$ and $KMnO_4$ with a $1:0.5$ molar ratio were mixed with 0.09 M of sodium hydroxide and 5 mL of water. The mixture was filled into a hardened stainless-steel grinding bowl (inner diameter: 7.5 mm – volume: 250 mL) of a Planetary Mono Mill Pulverisette 6 (Fritsch GmbH, Germany) ball-miller equipped with twenty-five hardened stainless-steel grinding balls of 4 g weight and 10 mm diameter. The mixture was milled at a speed of 200 rpm, 450 rpm and 600 rpm for 4 hours. The products were washed with water and freeze-dried for a night (>8 hours). The resulting products were labelled as M200, M450, and M600 corresponding to manganese-oxide samples prepared with 200 rpm, 450 rpm and 600 rpm milling speeds, respectively.	M200 M450 **M600**
Ball milling (metal-doped samples)	0.0005 M platinum(IV) chloride or 0.0005 M copper(II) chloride was added into the mixture of the manganese-oxide precursors before the milling process. The same quantity of precursors, milling time and milling speeds (200 rpm, 450 rpm and 600 rpm) were used as in the case of the pure manganese-oxide based catalysts. The final product was obtained after filtration, washing with water followed by freeze-drying overnight.	M200(Cu-milled) M450(Cu-milled) M600(Cu-milled) M200(Pt-milled) M450(Pt-milled) **M600(Pt-milled)**
Pt loading by wet impregnation method	The required amount of $H_2PtCl_6 \cdot xH_2O$ (to reach three wt% of metallic Pt) was dissolved into a determined amount of ethanol. The ethanoluous solution was filtrated into the pores of the M600 manganese oxide support. The supported catalyst was dried overnight.	**M600(Pt-impregnated)**
5 nm Pt loading by sonication	First, 5 nm Pt nanoparticles with controlled size were produced.[48] Here, 0.04 g of platinum(II) acetylacetonate and 0.035 g of polyvinylpyrrolidone (PVP, $M_W = 40\,000$) were dissolved in 5 mL of ethylene-glycol and ultrasonicated for 30 minutes to obtain a homogenous solution. The solution was poured into a three-necked round bottom flask and was evacuated and purged under atmospheric pressure argon gas for several cycles to get rid of additional oxygen and water. After three purging cycles, the flask was immersed into an oil bath heated up to 473 K under vigorous stirring of the reaction mixture as well as the oil bath. After 10 minutes of the reaction, the flask was cooled down to room temperature. The suspension was precipitated by centrifugation with the co-addition of acetone to the reaction mixture. The nanoparticles were washed by centrifuging with hexane and redispersing in ethanol for at least 2–3 cycles and finally redispersed in ethanol. The concentration of the Pt nanoparticles was measured using an ICP technique. To fabricate manganese-oxide supported Pt nanoparticle catalysts, the ethanoluous suspension of 5 nm Pt nanoparticles and M600 manganese oxide were mixed in ethanol and sonicated in an ultrasonic bath (40 kHz, 80 W) for 3 hours.[6] The supported nanoparticles were collected by centrifugation. The products were washed with ethanol three times before they were left for a night (>8 hours) to dry at a temperature of 353 K.	**M600(5 nm Pt-sonicated)**

Hydrogenation of carbon dioxide in a continuous flow reactor. Catalytic reactions were carried out at atmospheric pressure in a fixed-bed continuous-flow reactor (200 mm long with 8 mm i.d.) and heated externally.[50] The dead volume of the reactor was filled with quartz beads. The operating temperature was controlled by a thermocouple placed inside the oven close to the reactor wall, to ensure precise temperature measurement. For catalytic studies, small fragments (about 1 mm) of slightly compressed pellets were used. Typically, the reactor filling contained 150 mg of the catalyst. In the reacting gas mixture, the $CO_2:H_2$ molar ratio was $1:4$, if not denoted otherwise. The $CO_2:H_2$ mixture fed with the help of mass flow controllers (Aalborg), the total flow rate was 50 ml min^{-1}. The reacting gas mixture flow entered and left the reactor through an externally heated tube to avoid condensation. Agilent 6890N gas chromatography analysis of the products and reactants was carried out using an HP-PLOTQ column. The gases were detected simultaneously by thermal conductivity (TC) and flame ionisation (FI) detectors. The CO_2 was transformed to methane using a methanizer before being analyzed by FID.

3 Results and discussion

3.1 Mechanochemical synthesis and energy calculation

Fig. 1a represents the high-energy ball milling process. Furthermore, the milling-map of samples milled with different rotation speeds of 200 rpm (M200), 450 rpm (M450), and 600 rpm (M600) are shown in Fig. 1b where the ball-impact energy (E_b)[51,52] and cumulative energy (E_{cum}) were calculated using eqn (1) and (2), respectively.[51–55] This model allows the calculation of the impact energy of a single ball hit event as well as the amount of the total energy transferred to the milled material during the process. By comparing the results from a simple statistical model with those of the "Burgio–Rojac model",[52] we were able to demonstrate that the latter provides a more appropriate framework for the interpretation of milling-induced changes in manganese oxide at different oxidation states.

$$\Delta E_b^* = \frac{1}{2} \cdot \varphi_b \cdot K_a \cdot \left(\rho_b \frac{\pi d_b^3}{6} \right) \cdot W_p^2 \left(\left(\frac{W_v}{W_p} \right)^2 \left(\frac{D_v - d_b}{2} \right)^2 \right.$$

$$\left. \left(1 - 2\frac{W_v}{W_p} \right) - 2R_p \left(\frac{W_v}{W_p} \right) \left(\frac{D_v - d_b}{2} \right) - \left(\frac{W_v}{W_p} \right)^2 \left(\frac{D_v - d_b}{2} \right)^2 \right),$$

(1)

where "K" is the constant of the mill, "φ" is the obstruction coefficient and the other variables are the geometrical parameters of the mill and the milling drum. By modifying eqn (1) with the frequency of the impacts (ν), the milling time (t) and the measured material's mass (m_p), the cumulative energy (E_{cum}) from eqn (2) was calculated. It shows the energy value that is given off to one gram of the milled material.

$$E_{cum} = (\Delta E_b^* \cdot \nu_t \cdot t)/m_p \qquad (2)$$

This journal is © the Owner Societies 2020

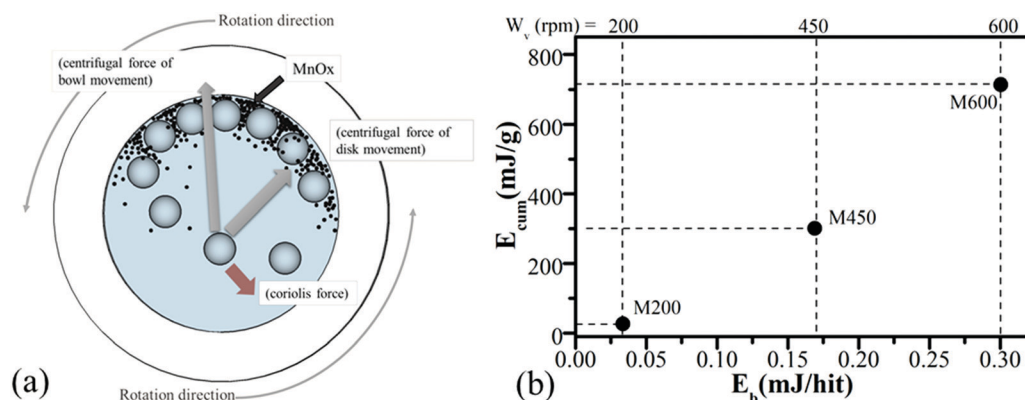*Phys. Chem. Chem. Phys.*, 2020, **22**, 13999–14012 | **14001**

Fig. 1 Schematic view of the motion of the ball and powder mixture in the high-energy ball milling process (a) and milling-map of the samples, displaying the grounding process with different ball-impact (E_b) and cumulative energy (E_{cum}) which is dependent on the rotational speed (W_v) (b). All the samples were milled for 4 hours.

By using the as-calculated E_b and E_{cum} energies, milling-maps were made, to illustrate the changes in each sample (M200, M450 and M600). As shown in Fig. 1b, as the rotation speed increases, the ball impact energy (E_b) and cumulative energy (E_{cum}) both increased by a certain amount, which affects the crystal structure and physical–chemical properties of the samples. The following sections (3.2 and 3.3) will describe the crystal structure, chemical and morphological characterization of the samples.

3.2 Structural determination and chemical characterization

Fig. 2a shows the X-ray diffraction patterns of the milled samples. The main reflection peaks of the sample milled at 200 rpm (M200) are at 12.4°, 25.1°, 36.9° and 65.4°, and they correlate with birnessite type σ-MnO$_2$ (JCPDS 421317).[56,57] The reflection peaks of the sample milled at 450 rpm (M450) are at 12.4°, 25.3°, 36.5°, 44.6° and 65.4° and they refer to birnessite type σ-MnO$_2$ (JCPDS 421317),[58] furthermore, hausmannite-type amorphous Mn$_3$O$_4$ (JCPDS 011127)[59] could be detected at 44.6°. The sample milled at 600 rpm (M600) showed only three major reflection peaks at 36.2°, 44.6° and 64.6°, which match with amorphous Mn$_3$O$_4$ (JCPDS 011127).[59,60] The crystal structure tuned by birnessite type manganese(IV) oxide (M200) reduces to manganese(III and II) oxides in the case of M450 and M600

samples under alkaline conditions during the milling process. As the rotation speed increases, the energies (E_b and E_{cum}) increase as well and the temperature rises slightly inside (reference) the milling chamber. Consequently, the interlayer water is partially released, which weakens the layered structure.

Fig. 2b shows the Raman spectra of the samples, where the characteristic Raman shifts of the Mn–O symmetric stretching vibration at 647 cm^{-1} could be observed for all three manganese oxides. The shift at 575 cm^{-1} originates from the Mn–O symmetric stretching vibration in the basal plane of [MnO$_6$] sheets of birnessite, and it is dependent on the presence of Mn^{4+} ions in sample M200 and M450, respectively.[61] In the case of M600, which is an amorphous hausmannite-type manganese oxide,[62] the Raman shift at 575 cm^{-1} is absent due to the total transformation of Mn(IV) into Mn^{3+} and Mn^{2+} ions in the structure.

X-ray diffraction patterns of the metal (Pt and Cu) doped samples and their Raman shifts are shown in the ESI† (Fig. S1 and S2). No additional peaks were observed in the doped samples for both measurements, which illustrates that loading during the milling process does not alter the original crystal structure of the manganese oxides. One thing to note regarding the Raman spectra: the ratio of the Mn–O liberal stretching and the Mn–O basal plane stretching of the M200 samples are slightly fluctuating due to the Pt or Cu atoms in their structure.
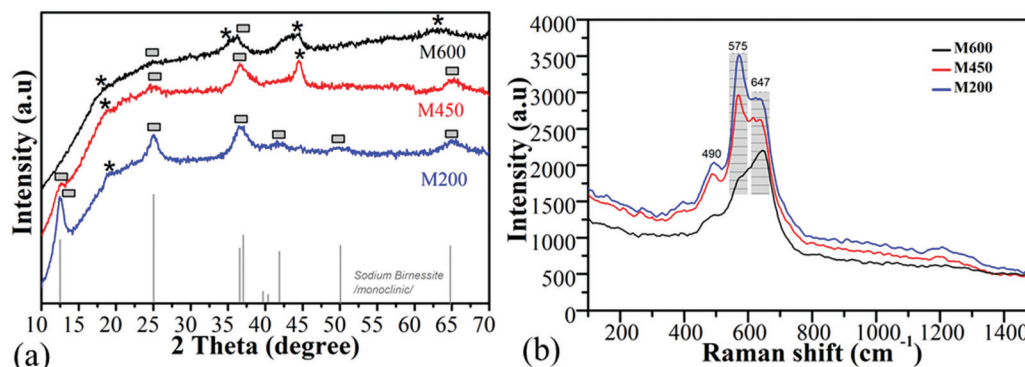

Fig. 2 X-ray diffraction patterns of the pure samples (a) {* birnessite type σ-MnO$_2$, ■ Mn$_3$O$_4$ phase} and the Raman spectra of the samples (b).

14002 | *Phys. Chem. Chem. Phys.*, 2020, **22**, 13999–14012

This journal is © the Owner Societies 2020

Fig. S3 (ESI†) shows the energy-dispersive X-ray spectra and the elemental analysis results are summarized in Table S1 (ESI†). The EDS spectra reveal that the samples consisted of oxygen, manganese, potassium, sodium, and doped metal elements only, and no impurities from the milling bowl and balls can be found (Fig. S3, ESI†). The sodium and potassium contents were decreased from 0.9 atomic percentage (at%) and 6.51 (at%) to 0.11 (at%) and 2.64 (at%), respectively as the milling speed was increased from 200 rpm to 600 rpm. The presence of a Pt-dopant resulted in a ~14 times higher sodium and potassium content in the Pt-doped M600 sample compared to the pure M600 sample. The weight percentage of the Pt in M600 (Pt-milled) was ~3 (wt%) proving that the Pt atoms were fully incorporated into the structures confirming the weight ratio from the precursors (Table S1, ESI†).

3.3 Morphological characterization

Fig. 3a displays the results of the specific surface area measurements. The surface area of the sample was dependent on the milling speed, and it increased from 11 $m^2\ g^{-1}$ to 150 $m^2\ g^{-1}$ for M200 and both M450, and M600, as presented in Table 2. M200 had mostly micropores, while M450 and M600 were mesoporous with an average pore radius of ~6 nm (Fig. S4, ESI†). Manganese-oxides milled at a higher milling speed (M450 and M600) presented a higher average specific surface area than the manganese-oxide nanoparticles observed in the literature.[63,64]

Fig. 3b shows the results of the thermogravimetric analysis of the samples under air. The main thermal changes in the M200 and M450 samples are similar to typical synthetic birnessites. During the first decomposition step at RT – 110 °C a weight loss of ~6% was caused by the release of physically adsorbed water.[65] The second weight loss of ~2% resulted at 220 °C stemming from the release of physically adsorbed water from the interlayer spacing.[66] The third weight loss occurred at 500 °C and 570 °C for M200 and M450, respectively, corresponding to the reduction of Mn(IV) to Mn(III, II) and the formation of Mn_2O_3.[67] The fourth change occurred around 550 °C and 630 °C for M200 and M450, respectively, where a 1% weight gain occurred due to the slow re-oxidation of the manganese Mn_3O_4 to Mn_2O_3 and α-MnO_2.[68,69] It is interesting to note that only in the

Table 2 Specific surface area results of the ball-milled manganese-oxide samples

Samples	Specific surface area, $m^2\ g^{-1}$	Pore radius, nm	Pore volume, cc g^{-1}
M200	11	<2	0.06
M450	159	>5.7	0.7
M600	159	>5.8	0.6

case of the M200 sample, did a fifth thermal change occur where the rest of the Mn_2O_3 reduced to Mn_3O_4 at 680 °C.[70]

On the other hand, the thermal decomposition behaviour was quite different for the M600 sample due to the presence of Mn(II, III)-oxide phases. The first decomposition occurred at 110 °C with ~4 wt% weight loss, which corresponds to the release of physically adsorbed water. The second change occurred with ~1% weight gain at 200 °C possibly stemming from the oxidation of manganese and phase change of Mn_3O_4 to Mn_2O_3.[68] The third change was a weight loss of ~2% due to the reduction of Mn_2O_3 to Mn_3O_4.[70] Oxidation occurred at a low temperature for the M600 sample, which indicates that the amount of Mn(III) is much higher than in the other two samples. It also demonstrates slow crystallization of the amorphous morphology.[65] Fig. S5(a–d) (ESI†) discloses the thermogravimetric analysis under a nitrogen flow. No weight loss or gain occurred at 300–550 °C for the M600 sample in a nitrogen flow, helping to prove the results and discussion about the thermal analysis under air.

In Fig. S6a (ESI†), X-ray diffraction patterns of the samples after TG analysis under both air and nitrogen atmospheres showed that α-MnO_2 and Mn_3O_4 oxides were produced by thermal analysis in air, while only Mn_3O_4 remained for M200. In the case of the M450 sample, α-MnO_2 and Mn_3O_4 phases formed, compared to M600, where only Mn_3O_4 was created under oxidative conditions. From the thermogravimetric analysis of the samples and the X-ray diffraction patterns of the end products (after TGA), we can derive the same conclusion from the diffraction patterns of the initial samples, such as M200 is mainly consisted of MnO_2 (manganese oxidation state: 4+), and M450 consists of MnO_2 and a minor amount of Mn_3O_4 (manganese oxidation state: IV, III, II), while M600 consists of an almost pure phase Mn_3O_4 (manganese oxidation state: III, II).
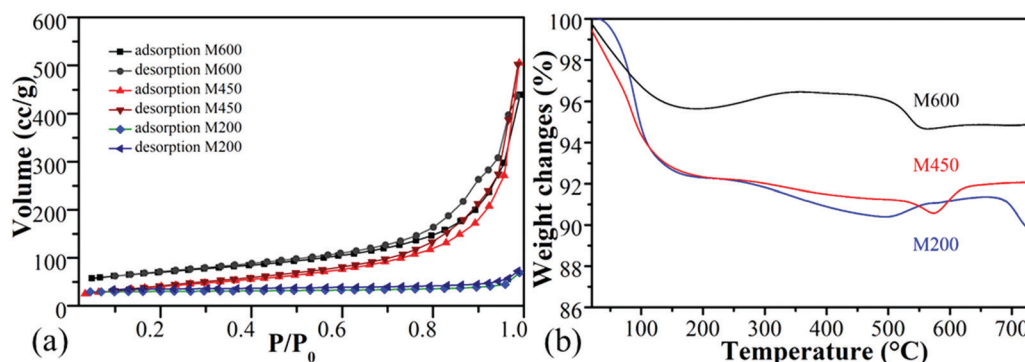

Fig. 3 N$_2$ adsorption analysis full isotherm (a) and thermal decomposition of the pure samples at a heating rate of 5 °C min^{-1} in air (b).

This journal is © the Owner Societies 2020

Phys. Chem. Chem. Phys., 2020, **22**, 13999–14012 | **14003**

Fig. S5e (ESI†) presents the differential scanning calorimetric results of the samples. During the heating process at low temperature (150 °C), endothermic peaks appear for M200 and M450 related to the dehydration of interlayer water and the formation of Mn_2O_3. Endothermic peaks at higher temperatures illustrate the reduction of Mn(III) to Mn(II) and the possible phase transition to tunnel-structured flakes of Mn_3O_4.[71] In the case of M600, one endothermic peak observed around 550 °C illustrates the phase transition of Mn_3O_4 from an amorphous state to a nanoflake structure.

Fig. 4(a, c, e) and (b, d, f) show the scanning electron microscopy (SEM) and transmission electron microscopy images, respectively. With the increment of the milling speed, the average particle size also decreased. The M200 sample has larger flakes and aggregated sheets identical to a typical birnessite-structure,[35] while at higher milling speeds, the crystal structure was ruined due to the higher mechanical impact as well as the higher temperature resulting in the decreases in the interlayer water. Besides the fact that the average oxidation state of manganese decreased in the case of the M450 and M600 samples compared to the M200 sample, the structure of the M450 sample consisted of a mixture of sheets and flakes and M600 consisted mostly of 10–50 nm small nanoflakes.[72]

4 The catalytic CO_2 hydrogenation reaction

Manganese oxides prepared at different milling speeds as well as several Pt- and Cu-doped (loaded with ball milling, wet impregnation method and ultrasonication assisted addition of nanoparticles) manganese oxides tested in CO_2 hydrogenation to form carbon-monoxide and methane at 573–823 K in a fixed-bed continuous-flow catalytic reactor at ambient pressure. The catalytic activity was monitored by the consumption rate and selectivity, which is discussed in the following sections. The reaction rates and calculated activation energies for CO_2 hydrogenation reactions over all samples are summarized in Table 3.

4.1 Effect of milling speed

All the ball-milled manganese oxide prepared at different milling speeds (M200, M450, M600) were active in the CO_2 hydrogenation reaction at >600 K and was producing mostly carbon-monoxide besides a small amount of methane (Fig. 5a). In the case of the reaction tested at 873 K, the M600 catalysts showed the highest CO_2 consumption rate ($\sim 20\,000$ nmol g^{-1} s^{-1}) followed by M450 (17 500 nmol g^{-1} s^{-1}). Both M600 and M450
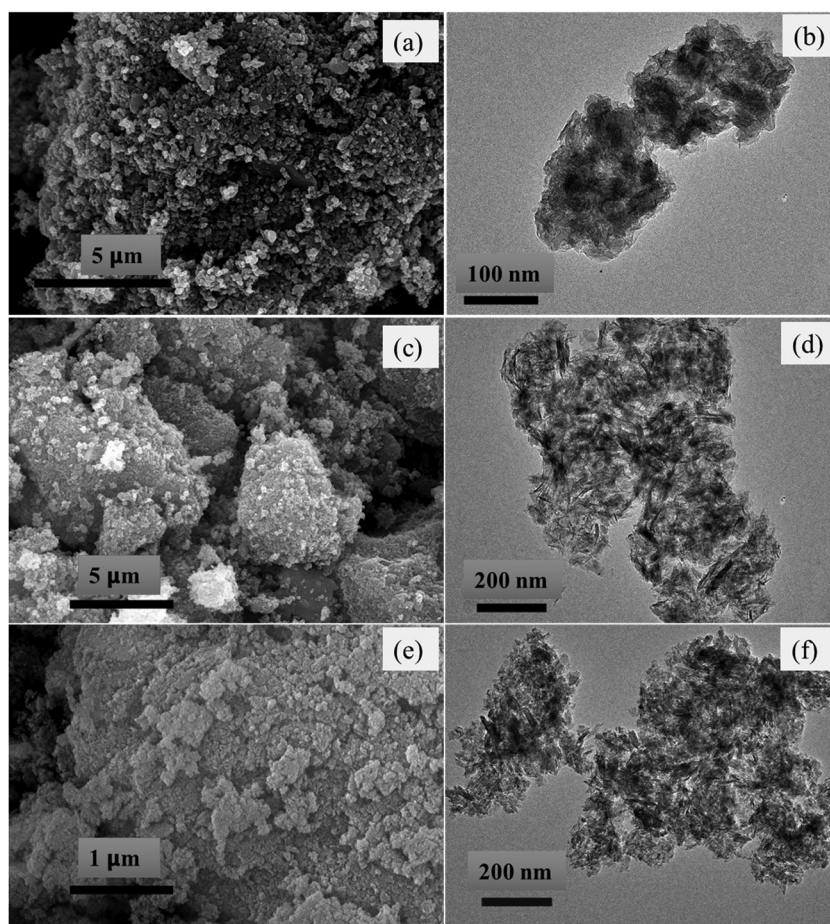

Fig. 4 Scanning electron microscopy images (SEM) and transmission electron microscopy (TEM) images of the pure samples (a and b) M200, (c and d) M450 and (e and f) M600.

14004 | *Phys. Chem. Chem. Phys.*, 2020, **22**, 13999–14012

This journal is © the Owner Societies 2020

Table 3 Reaction rates (at 673 K and 873 K) and the activation energies for CO_2 hydrogenation reactions over the samples at 873 K

Sample name	CO_2 consumption rate, nmol g^{-1} s^{-1}		Activation energy, kcal mol^{-1}
	673 K	873 K	
M200	—	10 083	54.9
M450	1038	16 707	23.7
M600	1954	19 523	19.3
M200(Cu-milled)	2811	19 430	19.7
M450(Cu-milled)	3367	19 129	16.0
M600(Cu-milled)	6943	20 722	16.7
M200(Pt-milled)	11 186	22 052	13.5
M450(Pt-milled)	14 293	22 338	11.2
M600(Pt-milled)	12 730	19 996	7.6
M600(Pt-impregnated)	9318	20 151	13.5
M600(5 nm Pt-sonicated)	9283	18 895	16.7

were almost two times more active compared to the catalyst milled at 200 rpm ($\sim 10\,000$ nmol g^{-1} s^{-1}). The high activity of manganese-oxide milled at higher speeds can be attributed to the high specific surface area[73] and porosity as well as the morphological differences. Furthermore, the samples milled at different speeds after the pretreatment in hydrogen showed diversity in the ratio of $Mn^{4+} : Mn^{3+} : Mn^{2+}$ (Fig. S7a, ESI†), which could also affect the catalytic activity. After the pretreatment, the birnessite type σ-MnO_2 ratio decreased, and mostly amorphous or nanoscaled $Mn(II, III)_3O_4$ and $Mn(II)O$ presented in the catalyst before the reaction.

It is interesting to note that these kinds of noble metal-free oxides have unusual activity compared to mesoporous MnO_2

samples. Also, they are competitive with other metal-based (*e.g.*, Ni, Co) oxides in CO_2 activation.[6] M200, M450 and M600 were stable at 873 K under the reaction conditions for ~ 10 hours (Fig. 5b).

As the milling speed was increased, the activation energy of the reaction in the range of 573–873 K was decreased drastically showing the presence of different reaction pathways besides the increasing reaction rate (Table 3). The differences in pathways and reaction rates can be attributed to the different structures of manganese oxides (birnessite type σ-MnO_2 for M200, birnessite type σ-MnO_2 and hausmannite-type amorphous Mn_3O_4 for M450 and amorphous Mn_3O_4 for M600) as evidenced by the XRD results.

4.2 Effect of one-pot loading of Pt- and Cu-doped catalysts

To enhance the catalytic activity, we used a simple one-pot method to dope 3 wt% of Pt and Cu into the manganese oxide nano-structures during the milling process. The catalytic activity was significantly enhanced by adding Pt into the manganese oxide structure at 673 K (Fig. 6a). In the case of the Pt-doped manganese-oxide catalyst milled under different speeds, ~ 12–13 times incre-ment in the catalytic activity was observed, showing the presence of the significant role of Pt where the effect of the milling speed was insignificant. Cu-doping resulted in a ~ 2.5 times increment in the catalytic activity compared to the pure manganese-oxide catalysts.

At the higher temperature (873 K) displayed in Fig. 6b, the catalytic boosting effect of Pt, as well as Cu-doping, was negligible.
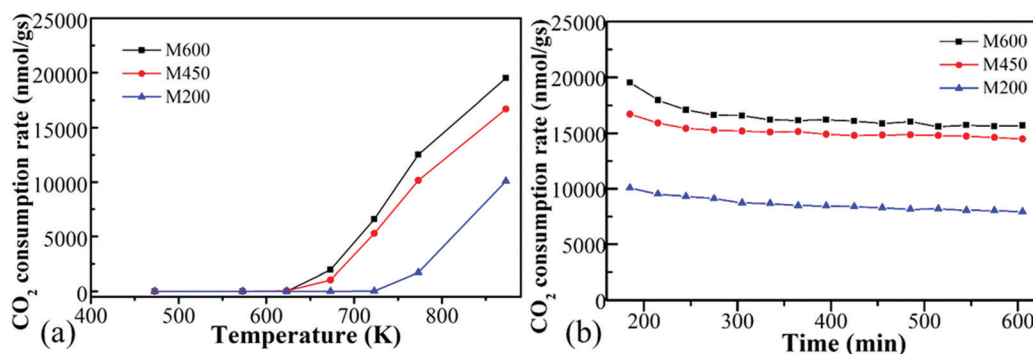
Fig. 5 The CO_2 consumption rate of manganese oxides synthesized by different milling speed (200 rpm-M200, 450 rpm-M450 and 600 rpm-M600) as a function of temperature (a) and function of time (b).
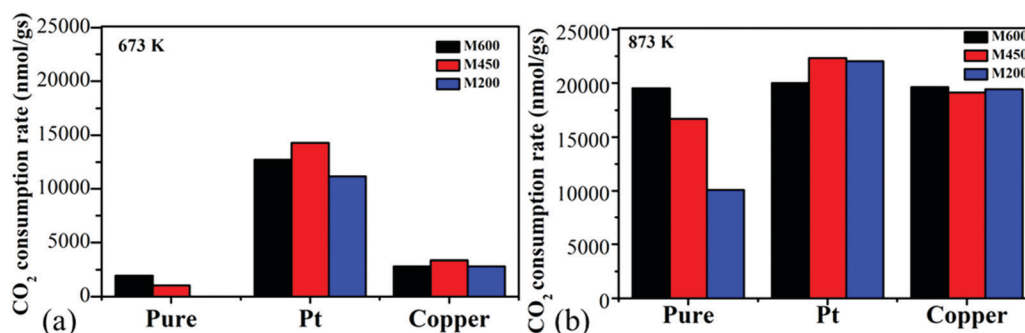
Fig. 6 Temperature effect for the CO_2 consumption rate of the samples at (a) 673 K and (b) 873 K.

All the metal-loaded catalysts showed similarly high activity ($\sim$20 000 nmol g^{-1} s^{-1}) as the pure manganese-oxide milled at 600 rpm. This phenomenon shows that the particular mixed Mn(IV, III, II)-oxide role is crucial in the catalytic activity at higher temperatures. These changes illustrate that temperature plays a vital role in the manganese oxide-based catalysts due to crystal structure changes and reducibility of the manganese oxides.

Both copper and platinum doping resulted in the decrease of the activation energy values (Table 3). As the milling speed was increased, the activation energy was decreased. Platinum showed lower values compared to copper-loaded samples.

4.3 Effect of Platinum incorporation (milling *vs.* impregnation *vs.* sonication)

Three different types of Pt-loaded M600 prepared by using one-pot synthesis, incipient wetness impregnation as well as loading of pre-synthesized 5 nm Pt nanoparticles to the catalysts by ultrasonication. All Pt-doped catalysts displayed almost the same catalytic activity (Fig. 7a and b). Usually, a wet impregnation method or even surfaces designed by adding size-controlled nanoparticles resulted in specific loading of the metal onto the surface as well as a catalytic activity increment.[74] These tests support the idea that the main working surface of these kinds of catalysts is based on the manganese-oxide, regardless of the quality and type of doped metal onto the surface.

It was interesting to note that the activation energies for these catalysts over the CO$_2$ activation showed differences; however, the reaction rate did not show big differences. The samples loaded with Pt prepared by milling showed the lowest activation energies (Table 3).

4.4 Selectivity towards methane

In the case of the selectivity, these catalysts mostly produced carbon monoxide ($>$95%) and a smaller amount of methane. Most catalysts started to produce methane with a small ratio at an elevated temperature ($\sim$623 K) and after a short increment, shifting of the products into the formation of carbon monoxide was observed (Fig. 8a) as expected from the thermodynamics of the CO$_2$ hydrogenation reaction in the gas phase.[6] In the case of the M600(Pt-milled) catalyst produced by the one-pot milling process, methane formation was significant compared to pure and Cu-loaded catalysts prepared by using different milling speeds. However, the results show that the catalytic activity is not profoundly influenced by the metal-loading, however, the Pt/MnO$_x$ interphase is crucial in the methane selectivity. The Pt-loaded manganese-oxide prepared *via* the one-pot synthesis has 1.5–2 times higher selectivity towards methane compared to the Pt-loaded MnO$_x$ catalyst synthesized by the wet impregnation and size-controlled Pt sonication, which shows the influence of the formed Pt/MnO$_x$ during the reaction (Fig. 8b).
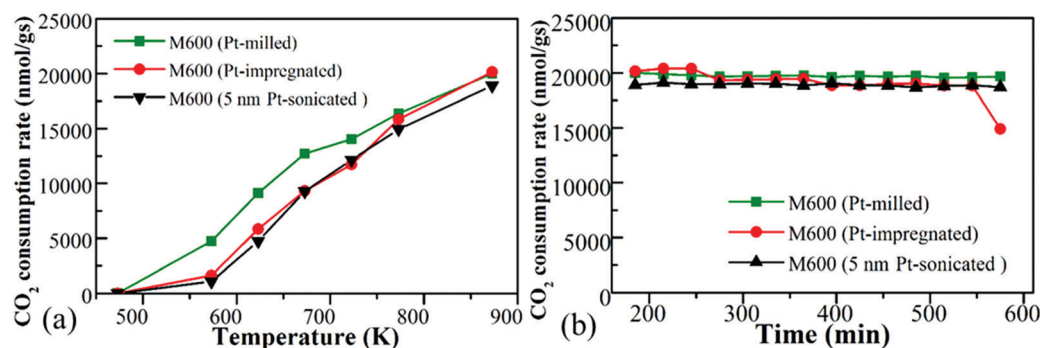

Fig. 7 The CO$_2$ consumption rate of the Pt-doped M600 manganese oxide prepared by the one-pot method, incipient wetness impregnation method as well as the designed incorporation of size-controlled 5 nm Pt nanoparticles as a function of temperature (a) and a function of time (b).
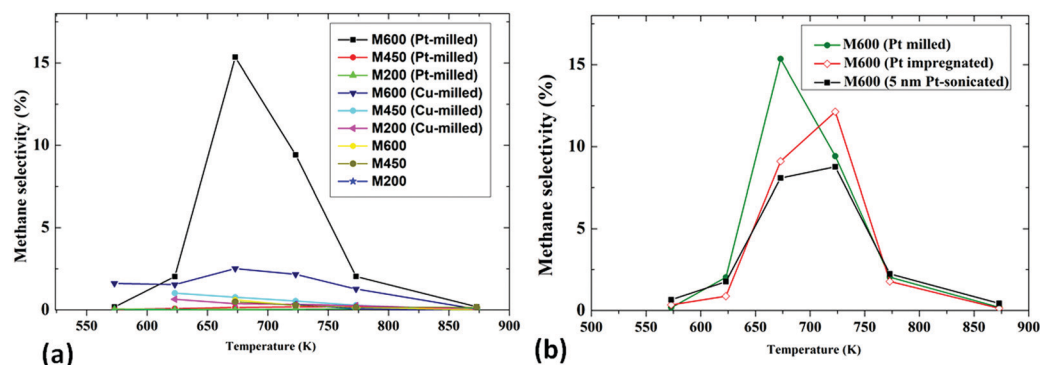

Fig. 8 The selectivity of methane during the CO$_2$ hydrogenation reaction in the case of (a) pure, Pt-loaded and Cu-loaded catalysts prepared by using different milling speeds and (b) M600 loaded with Pt by different methods.

14006 | *Phys. Chem. Chem. Phys.*, 2020, 22, 13999–14012

This journal is © the Owner Societies 2020

Table 4 The catalytic results of the Pt-loaded M600 at 673 K (one-pot milled, wet impregnated, and sonicated)

Catalyst	CO formation rate, nmol g^{-1} s^{-1}	CO formation selectivity, %	Methane formation rate, nmol g^{-1} s^{-1}	Methane formation selectivity, %
M600(Pt-milled)	12759	82	2362	15
M600(Pt-impregnated)	9716	89	992	9
M600(5 nm Pt-sonicated)	9229	90	822	8

Table 4 displays the formation rate and selectivity towards CO and CH_4 of 3 Pt-incorporated samples: M600(Pt-milled), M600(Pt-impregnated) and M600(5 nm Pt-sonicated) at 673 K. In the presence of Pt in the M600 catalyst prepared by the one-pot ball-milling process, the catalytic activity was ∼17 times higher at 673 K while it was similar at 823 K compared to the Pt-free M600 catalyst. While the main product was CO, the highest amount of CH_4 (∼20%) was formed in the case of the Pt-doped M600.

4.5 Determining the oxidation states (XPS data processing and evaluation) of the catalysts

For a better understanding of the activity differences of the catalysts, the oxidation states of the Mn species were investigated by *ex situ* XPS for samples prepared with low (M200) and high (M600) milling speeds as well as co-milled with Pt salts at 600 rpm (M600-Pt-milled) after the pretreatment of the samples in O_2 followed by H_2 at 300 °C as well as after the CO_2 hydrogenation reactions. The Mn 2p regions were fitted with multiplet states taken into consideration (Fig. S8, ESI†).[49] The ratios of the Mn oxidation states were calculated based on the peak areas of the fittings in Fig. 9. (Data values are summarized in Table S2, ESI.†)

Before the CO_2 hydrogenation (after the pretreatment), in the case of the M200 catalyst, Mn(III) and M(IV) presented with a ratio of Mn(III):Mn(IV) = ∼2. However, after the reaction, this ratio decreased to ∼1 showing the presence of the oxidation of the catalyst during the CO_2 hydrogenation. Usually, under the hydrogenation processes, the reduction of the surface is favourable,[6,50] but the possibility of CO_2 dissociation to CO and *O followed by the oxidation of the metallic or metal–oxide surface as well as the oxidation of the surface by H_2O resulting from the Reverse Water Gas Shift Reaction $(RWGSR−CO_2 + H_2 \Rightarrow CO + H_2O)$ can be also possible.[75,76] In the case of the M600 catalyst, a small amount of Mn(II)

(∼10%) was observed next to a higher amount of Mn(III) with the absence of Mn(IV) on the surface before the reaction. After the CO_2 hydrogenation reaction, the oxidation of the surface was observed as in the case of the M200 sample. The small amount of the Mn(II) was reduced to ∼3% and Mn(IV) appeared with a ratio of Mn(III):Mn(IV) = ∼3.

As we could see during the catalytic tests (Section 4.1), the M600 catalysts showed the highest CO_2 consumption rate and were almost two times more active compared to M200 at both low and high temperatures. We believe that beside the high specific surface area and porosity as well as the morphological differences, the Mn oxidation states play an important role during the reaction. In the case of the M600 sample, the presence of Mn(II) and the higher concentration of Mn(III) could be the reason for the higher catalytic activity. In manganese-based catalyst driven photosynthesis, the presence of $Mn(II)Mn(III)_3$ is needed for the production of the photo assembly intermediates and $Mn(III)Mn(IV)_3$ was responsible for the oxygen releasing step.[77] We also found in our recent studies that Mn(II) helped the reduction of CO_2 hydrogenation as a support for metallic Cobalt where the reaction followed the format pathway towards CH_4 production.[78] We believe that, the presence of Mn(II) as well as the ratio of Mn(III)/Mn(IV) is crucial for this reaction driven by manganese oxide-based catalysts.

Ex situ XPS data show that before the reaction, Mn(II) was observed with the content of ∼20% next to Mn(III). The higher amount of the reduced phase compared to the pure M600 shows the reducing effect of Pt under the H_2 pretreatment process. However, after the CO_2 activation, a huge amount of Mn(IV) was formed on the surface with a Mn(III)/Mn(IV) ratio of ∼1 beside the slight reduction of the content of Mn(II) to ∼18%. Beside the fact that the presence of Pt usually increases the activity of CO_2 reduction,[79,80] the perturbation of the Mn oxidation state by Pt can also affect the catalytic activity. At a lower temperature, the Pt-loading resulted in ∼17 times higher
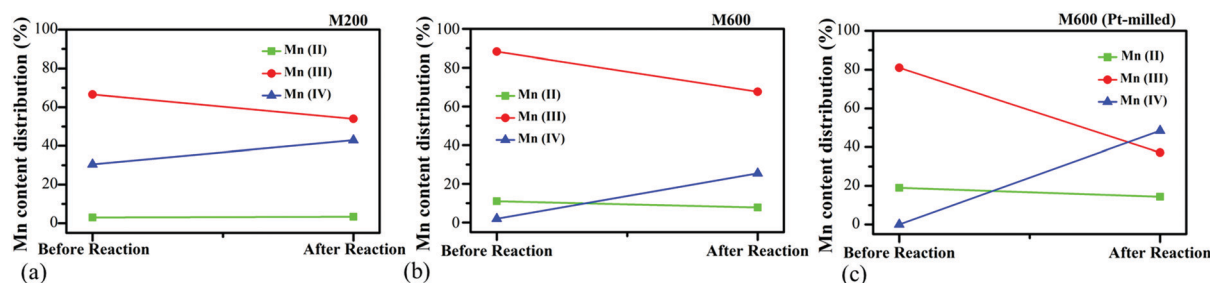
Fig. 9 Atomic ratios of Mn with different oxidation states before CO_2 hydrogenation (after pretreatment) and after CO_2 hydrogenation reactions for (a) M200, (b) M600, and (c) Pt-milled M600.

This journal is © the Owner Societies 2020

Phys. Chem. Chem. Phys., 2020, **22**, 13999–14012 | **14007**

Table 5 Comparison of CO_2 conversion percentage (Pt loaded samples) with previously published references at different temperatures

Catalyst	Synthetic method	Temperature, K	CO_2 conversion (%)	Ref.
M600(Pt-milled)	Ball milling	673	42	This study
M600(Pt-impregnated)	Ball milling/impregnation	673	28	This study
M600(5 nm Pt-sonicated)	Ball milling/sonication	673	28	This study
Pt/MnO_2	Hard template	648	25	6
MnO_x–Co_3O_4	Sol–gel inverse micelle	523	45	73
$PtCo/CeO_2$	—	573	6	81
K–Mn–Fe/Al_2O_3	Co-incipient wetness impregnation (IWI)	836	41	82
La–Mn–Zn–Cu–O	Sol–gel	543	13	83
Mn–Na/Fe	Co-precipitation	593	37	84
Pt/TiO_2	—	673	40	85
Fe/SiO_2-250	Wet impregnation	643	38	86
CuO–ZnO–Al_2O_3	Ball milling	523	12	87
Ni/SiO_2	Sol–gel	673	35	88

catalytic activity, where the CH_4 selectivity was drastically increased. This is interesting, as we know that usually, the presence of Pt helps to produce mostly CO in the CO_2 hydrogenation reaction.[50] On the other hand, at 823 K, the lack of the effect of Pt was observed in the catalytic activity compared to pure M600 catalysts. These phenomena can be attributed to the presence of Mn(II) as well as the different ratios of the oxidation states of the manganese in the oxides. In the future, we will focus on the atomic level understanding of such an easy-to-produce cheap catalyst to reach the highest activity by tuning the oxidation states of the manganese without using precious metals.

Furthermore, we summarized the comparison of the CO_2 conversion percentage of our Pt-loaded samples with previously published studies in Table 5. As seen in Table 5, our results prove that efficient manganese oxide catalyst synthesis can be done using a cost-effective one-pot ball milling method, and that even ball milling can be used as a simple method for the loading of metals.

5 Conclusions

A novel mechanochemical manganese oxide nanostructure synthesis was demonstrated, which can be easily scaled-up for synthetic industries. The shape, porosity, specific surface area, as well as the ratio of the different oxidation states of the Mn-ion in the structure, can be tuned by the milling speed. Pt-loaded and Cu-loaded MnO_x structures were prepared with the same one-pot technique and all the samples were tested in a CO_2 hydrogenation reaction in the gas phase. Pure MnO_x milled at 600 rpm milling speed showed the highest catalytic activity, and the effect of Pt-loading and Cu-loading was insignificant at higher temperatures. It showed that the presence of the different oxidation states of the manganese plays an essential role in the CO_2 activation process aside from the advantage of the higher surface area and porosity, which can be tuned by the milling speed of the ball milling process.

Also, Pt loading can improve methane selectivity. The one-pot synthesised Pt-loaded MnO_x nanostructure showed the highest methane selectivity compared to the Pt-loaded MnO_x catalyst synthesised by the wet impregnation and size-controlled Pt sonication, which shows the high impact of the formed Pt/MnO_x interface on the selectivity of the catalytic CO_2 hydrogenation reaction.

Conflicts of interest

There are no conflicts to declare.

Acknowledgements

Notes and references

1 N. S. Lewis and D. G. Nocera, Powering the Planet: Chemical Challenges in Solar Energy Utilization, *Proc. Natl. Acad. Sci. U. S. A.*, 2006, **103**(43), 15729–15735, DOI: 10.1073/pnas. 0603395103.

2 D. Bratt, *Catalytic CO_2 Hydrogenation – Literature Review: Technology Development since 2014*, 2016, https://hdl.handle. net/20.500.11919/779.

3 G. A. Olah, T. Mathew, A. Goeppert and G. K. S. Prakash, Difference and Significance of Regenerative Versus Renewable Carbon Fuels and Products, *Top. Catal.*, 2018, **61**(7), 522–529, DOI: 10.1007/s11244-018-0964-8.

4 J. Wei, Q. Ge, R. Yao, Z. Wen, C. Fang, L. Guo, H. Xu and J. Sun, Directly Converting CO_2 into a Gasoline Fuel, *Nat. Commun.*, 2017, **8**(May), 15174, DOI: 10.1038/ncomms15174.

5 C. Xie, C. Chen, Y. Yu, J. Su, Y. Li, G. A. Somorjai and P. Yang, Tandem Catalysis for CO_2 Hydrogenation to C2–C4 Hydrocarbons, *Nano Lett.*, 2017, **17**(6), 3798–3802, DOI: 10.1021/acs.nanolett.7b01139.

6 A. Sápi, T. Rajkumar, M. Ábel, A. Efremova, A. Grósz, A. Gyuris, K. B. Ábrahámné, I. Szenti, J. Kiss and T. Varga, *et al.*, Noble-Metal-Free and Pt Nanoparticles-Loaded, Mesoporous Oxides as Efficient Catalysts for CO_2 Hydrogenation and Dry Reforming with Methane, *J. CO$_2$ Util.*, 2019, **32**(January), 106–118, DOI: 10.1016/j.jcou.2019.04.004.

7 J. Martínez, E. Hernández, S. Alfaro, R. L. Medina, G. V. Aguilar, E. Albiter and M. A. Valenzuela, High Selectivity and Stability of Nickel Catalysts for CO_2 Methanation: Support Effects, *Catalysts*, 2019, **9**, 24, DOI: 10.3390/catal9010024.

8 H. Yang, C. Zhang, P. Gao, H. Wang, X. Li, L. Zhong, W. Wei and Y. Sun, A Review of the Catalytic Hydrogenation of Carbon Dioxide into Value-Added Hydrocarbons, *Catal. Sci. Technol.*, 2017, **7**(20), 4580–4598, DOI: 10.1039/c7cy01403a.

9 F. Studt, I. Sharafutdinov, F. Abild-Pedersen, C. F. Elkjær, J. S. Hummelshøj, S. Dahl, I. Chorkendorff and J. K. Nørskov, Discovery of a Ni–Ga Catalyst for Carbon Dioxide Reduction to Methanol, *Nat. Chem.*, 2014, **6**(4), 320–324, DOI: 10.1038/nchem.1873.

10 X. Du, D. Zhang, L. Shi, R. Gao and J. Zhang, Morphology Dependence of Catalytic Properties of Ni/CeO$_2$ Nanostructures for Carbon Dioxide Reforming of Methane, *J. Phys. Chem. C*, 2012, **116**(18), 10009–10016, DOI: 10.1021/jp300543r.

11 D. Shi, R. Wojcieszak, S. Paul and E. Marceau, Ni Promotion by Fe: What Benefits for Catalytic Hydrogenation?, *Catalysts*, 2019, **9**, 451, DOI: 10.3390/catal9050451.

12 S. Kar, A. Goeppert, J. Kothandaraman and G. K. S. Prakash, Manganese-Catalyzed Sequential Hydrogenation of CO_2 to Methanol via Formamide, *ACS Catal.*, 2017, **7**(9), 6347–6351, DOI: 10.1021/acscatal.7b02066.

13 C.-S. Li, G. Melaet, W. T. Ralston, K. An, C. Brooks, Y. Ye, Y.-S. Liu, J. Zhu, J. Guo and S. Alayoglu, *et al.*, High-Performance Hybrid Oxide Catalyst of Manganese and Cobalt for Low-Pressure Methanol Synthesis, *Nat. Commun.*, 2015, **6**, 6538, DOI: 10.1038/ncomms7538.

14 S. Lee and H. Xu, XRD and Tem Studies on Nanophase Manganese Oxides in Freshwater Ferromanganese Nodules from Green Bay, Lake Michigan, *Clays Clay Miner.*, 2016, **64**(5), 523–536, DOI: 10.1346/CCMN.2016.064032.

15 J. E. Post, Manganese Oxide Minerals: Crystal Structures and Economic And, *Proc. Natl. Acad. Sci. U. S. A.*, 1999, **96**(March), 3447–3454.

16 X. Huang, T. Chen, X. Zou, M. Zhu, D. Chen and M. Pan, The Adsorption of Cd(II) on Manganese Oxide Investigated by Batch and Modeling Techniques, *Int. J. Environ. Res. Public Health*, 2017, **14**(10), 1145, DOI: 10.3390/ijerph14101145.

17 Y. Xin Zhang, X. Long Guo, M. Huang, X. Dong Hao, Y. Yuan and C. Hua, Engineering Birnessite-Type MnO_2 nanosheets on Fiberglass for PH-Dependent Degradation of Methylene Blue, *J. Phys. Chem. Solids*, 2015, **83**, 40–46, DOI: 10.1016/j.jpcs.2015.03.015.

18 Y. Gorlin, B. Lassalle-Kaiser, J. D. Benck, S. Gul, S. M. Webb, V. K. Yachandra, J. Yano and T. F. Jaramillo, In Situ X-Ray Absorption Spectroscopy Investigation of a Bifunctional Manganese Oxide Catalyst with High Activity for Electrochemical Water Oxidation and Oxygen Reduction, *J. Am. Chem. Soc.*, 2013, **135**(23), 8525, DOI: 10.1021/ja3104632.

19 A. C. Thenuwara, S. L. Shumlas, N. H. Attanayake, E. B. Cerkez, I. G. McKendry, L. Frazer, E. Borguet, Q. Kang, M. J. Zdilla and J. Sun, *et al.*, Copper-Intercalated Birnessite as a Water Oxidation Catalyst, *Langmuir*, 2015, **31**(46), 12807–12813, DOI: 10.1021/acs.langmuir.5b02936.

20 W. Wang, Z. Shao, Y. Liu and G. Wang, Removal of Multi-Heavy Metals Using Biogenic Manganese Oxides Generated by a Deep-Sea Sedimentary Bacterium - Brachybacterium Sp. Strain Mn32, *Microbiology*, 2009, **155**(6), 1989–1996, DOI: 10.1099/mic.0.024141-0.

21 H. Guan, W. Dang, G. Chen, C. Dong and Y. Wang, RGO/KMn_8O_{16} composite as Supercapacitor Electrode with High Specific Capacitance, *Ceram. Int.*, 2016, **42**(4), 5195–5202, DOI: 10.1016/j.ceramint.2015.12.043.

22 T. B. Atwater and A. J. Salkind, *Lithium Potassium Manganese Mixed Metal Oxide Material for Rechargeable Electrochemical Cells*, Report of US Army Research Development & Engineering Comd (RDECOM), 2010, pp. 4–8.

23 S. Kattel, B. Yan, J. G. Chen and P. Liu, CO_2 Hydrogenation on Pt, Pt/SiO$_2$ and Pt/TiO$_2$: Importance of Synergy between Pt and Oxide Support, *J. Catal.*, 2016, **343**, 115–126, DOI: 10.1016/j.jcat.2015.12.019.

24 J. Nakamura, T. Fujitani, S. Kuld, S. Helveg, I. Chorkendorff and J. Sehested, Comment on "Active Sites for CO_2 Hydrogenation to Methanol on Cu/ZnO Catalysts", *Science*, 2017, **357**(6354), 1296–1299, DOI: 10.1126/science.aan8074.

25 X. Duan, J. Yang, H. Gao, J. Ma, L. Jiao and W. Zheng, Controllable Hydrothermal Synthesis of Manganese Dioxide Nanostructures: Shape Evolution, Growth Mechanism and Electrochemical Properties, *CrystEngComm*, 2012, **14**(12), 4196–4204, DOI: 10.1039/c2ce06587h.

26 Y. F. Liu, G. H. Yuan, Z. H. Jiang and Z. P. Yao, Solvothermal Synthesis of Mn_3O_4 Nanoparticle/Graphene Sheet Composites and Their Supercapacitive Properties, *J. Nanomater.*, 2014, **2014**, 190529, DOI: 10.1155/2014/190529.

27 Q. Zhang, J. Luo, E. Vileno and S. L. Suib, Synthesis of Cryptomelane-Type Manganese Oxides by Microwave Heating, *Chem. Mater.*, 1997, **9**(10), 2090–2095, DOI: 10.1021/cm970129g.

28 W. Thanthamrong, R. Songsak, D. Paweena, J. Wirat and W. Winadda, Electrodeposition of Manganese Oxide Nanosheets as Supercapacitor Electrode Materials, *Key Eng. Mater.*, 2016, **675–676**, 273–276, DOI: 10.4028/www.scientific.net/KEM.675-676.273.

29 C. Xu, S. De, A. M. Balu, M. Ojeda and R. Luque, Mechanochemical Synthesis of Advanced Nanomaterials for Catalytic Applications, *Chem. Commun.*, 2015, **51**(31), 6698–6713, DOI: 10.1039/c4cc09876e.

30 R. A. Buyanov, V. V. Molchanov and V. V. Boldyrev, Mechanochemical Activation as a Tool of Increasing Catalytic Activity,

This journal is © the Owner Societies 2020

Phys. Chem. Chem. Phys., 2020, **22**, 13999–14012 | **14009**

Catal. Today, 2009, 144(3–4), 212–218, DOI: 10.1016/j.cattod.2009.02.042.

31 P. Baláž, Mechanochemistry in Nanoscience and Minerals Engineering, Springer, 2008, pp. 103–132, DOI: 10.1007/978-3-540-74855-7.

32 S. Ostovar, A. Franco, A. R. Puente-Santiago, M. Pinilla-de Dios, D. Rodríguez-Padrón, H. R. Shaterian and R. Luque, Efficient Mechanochemical Bifunctional Nanocatalysts for the Conversion of Isoeugenol to Vanillin, Front. Chem., 2018, 6(APR), 1–7, DOI: 10.3389/fchem.2018.00077.

33 V. V. Molchanov and R. A. Buyanov, Mechanochemistry of Catalysts, Usp. Khim, 2000, 69(5), 490–493, DOI: 10.1070/rc2000v069n05abeh000555.

34 A. Gagrani, J. Zhou and T. Tsuzuki, Solvent Free Mechanochemical Synthesis of MnO$_2$ for the Efficient Degradation of Rhodamine-B, Ceram. Int., 2018, 44(5), 4694–4698, DOI: 10.1016/j.ceramint.2017.12.050.

35 H. Liu and K. Zhao, Asymmetric Flow Electrochemical Capacitor with High Energy Densities Based on Birnessite-Type Manganese Oxide Nanosheets and Activated Carbon Slurries, J. Mater. Sci., 2016, 51(20), 9306–9313, DOI: 10.1007/s10853-016-0177-0.

36 A. Iyer, P. Dutta and S. Suib, Water Oxidation Catalysis Using Amorphous Manganese Oxides, Octahedral Molecular Sieves (OMS-2), and Octahedral Layered (OL-1) Manganese Oxide Structures, J. Phys. Chem. C, 2012, 116, 6474–6483.

37 S. Anandan, B. Gnana Sundara Raj, G. J. Lee and J. J. Wu, Sonochemical Synthesis of Manganese(II) Hydroxide for Supercapacitor Applications, Mater. Res. Bull., 2013, 48(9), 3357–3361, DOI: 10.1016/j.materresbull.2013.05.021.

38 T. Prasad Yadav, R. Manohar Yadav and D. Pratap Singh, Mechanical Milling: A Top Down Approach for the Synthesis of Nanomaterials and Nanocomposites, Nanosci. Nanotechnol., 2012, 2(3), 22–48, DOI: 10.5923/j.nn.20120203.01.

39 T. N. Afonasenko, O. A. Bulavchenko, O. A. Knyazheva, O. N. Baklanova, T. I. Gulyaeva, M. V. Trenikhin, S. V. Tsybulya and P. G. Tsyrul'nikov, Effect of the Mechanical Activation of a Mixture of MnCO$_3$·mMn(OH)$_2$·nH$_2$O and AlOOH as a Stage of the Preparation of a MnO$_x$-Al$_2$O$_3$ Catalyst on Its Phase Composition and Catalytic Activity in CO Oxidation, Kinet. Catal., 2015, 56(3), 359–368, DOI: 10.1134/S0023158415030015.

40 O. A. Bulavchenko, T. N. Afonasenko, P. G. Tsyrul'nikov, O. A. Knyazheva, O. N. Baklanova and S. V. Tsybulya, MnO$_x$-Al$_2$O$_3$ Catalysts for Deep Oxidation Prepared with the Use of Mechanochemical Activation: The Effect of Synthesis Conditions on the Phase Composition and Catalytic Properties, Kinet. Catal., 2014, 55(5), 639–648, DOI: 10.1134/S0023158414050048.

41 V. V. Molchanov, V. V. Goidin, R. A. Buyanov, A. V. Tkachev and A. I. Lukashevich, Mechano-Chemical Reactions at High Pressure of the Gas Phase, Chemistry, 2002, 133–140.

42 Z. Sawlowicz, I. V. Bacherikova and S. M. Shcherbakov, The Effect of Mechanochemical and Ultrasonic Treatments CeO$_2$–MoO$_3$ = 1 : 1, Nanocomposites, Nanostrcutures and their application, Springer, 2019, ch. 8.

43 R. A. Buyanov, V. V. Molchanov and V. V. Boldyrev, Mechanochemical Activation for Resolving the Problems of Catalysis, KONA Powder Part. J., 2009, 27(27), 38–54, DOI: 10.14356/kona.2009007.

44 Z. J. Jiang, Z. H. Li, J. B. Yu and W. K. Su, Liquid-Assisted Grinding Accelerating: Suzuki-Miyaura Reaction of Aryl Chlorides under High-Speed Ball-Milling Conditions, J. Org. Chem., 2016, 81(20), 10049–10055, DOI: 10.1021/acs.joc.6b01938.

45 S. Zhuang, E. S. Lee, L. Lei, B. B. Nunna, L. Kuang and W. Zhang, Synthesis of Nitrogen-Doped Graphene Catalyst by High-Energy Wet Ball Milling for Electrochemical Systems, Int. J. Energy Res., 2016, 40(15), 2136–2149, DOI: 10.1002/er.3595.

46 V. Šepeĺak, Nanocrystalline Materials Prepared by Homogeneous and Heterogeneous Mechanochemical Reactions, Ann. Chim. Sci. des Mater., 2002, 27(6), 61–76, DOI: 10.1016/S0151-9107(02)90015-2.

47 V. V. Molchanov and R. A. Buyanov, Scientific Grounds for the Application of Mechanochemistry to Catalyst Preparation, Kinet. Catal., 2001, 42(3), 406–415, DOI: 10.1023/A:1010465315877.

48 A. Sápi, D. G. Dobó, D. Sebok, G. Halasi, K. L. Juhász, A. Szamosvölgyi, P. Pusztai, E. Varga, I. Kálomista and G. Galbács, et al., Silica Based Catalyst Supports Are Inert, Aren't They? – Striking Differences in Ethanol Decomposition Reaction Originated from Meso- and Surface Fine Structure Evidenced by Small Angle X-Ray Scattering, J. Phys. Chem. C, 2017, 121(9), 5130–5136, DOI: 10.1021/acs.jpcc.7b00034.

49 E. S. Ilton, J. E. Post, P. J. Heaney, F. T. Ling and S. N. Kerisit, XPS Determination of Mn Oxidation States in Mn (Hydr)-Oxides, Appl. Surf. Sci., 2016, 366, 475–485, DOI: 10.1016/j.apsusc.2015.12.159.

50 A. Sápi, G. Halasi, J. Kiss, D. G. Dobó, K. L. Juhász, V. J. Kolcsár, Z. Ferencz, G. Vári, V. Matolin and A. Erdöhelyi, et al., In Situ DRIFTS and NAP-XPS Exploration of the Complexity of CO$_2$ Hydrogenation over Size-Controlled Pt Nanoparticles Supported on Mesoporous NiO, J. Phys. Chem. C, 2018, 122(10), 5553–5565, DOI: 10.1021/acs.jpcc.8b00061.

51 N. Burgio, A. Iasonna, M. Magini, S. Martelli and F. Padella, Mechanical Alloying of the Fe-Zr System. Correlation between Input Energy and End Products, Nuovo Cimento D, 1991, 13(4), 459–476, DOI: 10.1007/BF02452130.

52 G. Kozma, R. Puskás, I. Z. Papp, P. Bélteky and Z. Kónya, Kukovecz. Experimental Validation of the Burgio-Rojac Model of Planetary Ball Milling by the Length Control of Multiwall Carbon Nanotubes, Carbon, 2016, 105, 615–621, DOI: 10.1016/j.carbon.2016.05.005.

53 T. Rojac, M. Kosec, B. Malič and J. Holc, The Application of a Milling Map in the Mechanochemical Synthesis of Ceramic Oxides, J. Eur. Ceram. Soc., 2006, 26(16), 3711–3716, DOI: 10.1016/j.jeurceramsoc.2005.11.013.

54 J. Joardar, S. K. Pabi and B. S. Murty, Milling Criteria for the Synthesis of Nanocrystalline NiAl by Mechanical Alloying, J. Alloys Compd., 2007, 429(1–2), 204–210, DOI: 10.1016/j.jallcom.2006.04.045.

14010 | Phys. Chem. Chem. Phys., 2020, 22, 13999–14012

This journal is © the Owner Societies 2020

55 C. X. Wu, S. G. Zhu, J. Ma and M. L. Zhang, Synthesis and Formation Mechanisms of Nanocomposite WC-MgO Powders by High-Energy Reactive Milling, *J. Alloys Compd.*, 2009, **478**(1–2), 615–619, DOI: 10.1016/j.jallcom.2008.11.100.

56 S. Qian, M. A. Cheney, R. Jose, A. Banerjee, P. K. Bhowmik and J. M. Okoh, Synthesis and Characterization of Birnessite and Cryptomelane Nanostructures in Presence of Hoffmeister Anions, *J. Nanomater.*, 2009, 940462, DOI: 10.1155/2009/940462.

57 J. Zhu and J. He, Facile Synthesis of Graphene-Wrapped Honeycomb MnO_2 Nanospheres and Their Application in Supercapacitors, *ACS Appl. Mater. Interfaces*, 2012, **4**(3), 1770–1776, DOI: 10.1021/am3000165.

58 J. Yan, Z. Fan, T. Wei, W. Qian, M. Zhang and F. Wei, Fast and Reversible Surface Redox Reaction of Graphene-MnO_2 Composites as Supercapacitor Electrodes, *Carbon*, 2010, **48**(13), 3825–3833, DOI: 10.1016/j.carbon.2010.06.047.

59 M. Aghazadeh, A. Bahrami-Samani, D. Gharailou, M. G. Maragheh, M. R. Ganjali and P. Norouzi, Mn_3O_4 Nanorods with Secondary Plate-like Nanostructures; Preparation, Characterization and Application as High Performance Electrode Material in Supercapacitors, *J. Mater. Sci.: Mater. Electron.*, 2016, **27**(11), 11192–11200, DOI: 10.1007/s10854-016-5239-1.

60 M. Fang, X. Tan, M. Liu, S. Kang, X. Hu and L. Zhang, Low-Temperature Synthesis of Mn_3O_4 Hollow-Tetra-kaidecahedrons and Their Application in Electrochemical Capacitors, *CrystEngComm*, 2011, **13**(15), 4915–4920, DOI: 10.1039/c1ce05337j.

61 C. Julien, M. Massot, R. Baddour-Hadjean, S. Franger, S. Bach and J. P. Pereira-Ramos, Raman Spectra of Birnessite Manganese Dioxides, *Solid State Ionics*, 2003, **159**(3–4), 345–356, DOI: 10.1016/S0167-2738(03)00035-3.

62 C. M. Julien, M. Massot and C. Poinsignon, Lattice Vibrations of Manganese Oxides: Part I. Periodic Structures, *Spectrochim. Acta, Part A*, 2004, **60**(3), 689–700, DOI: 10.1016/S1386-1425(03)00279-8.

63 H. Liu, H. Zhang, L. Shi, X. Hai and J. Ye, Lattice Oxygen Assisted Room-Temperature Catalytic Process: Secondary Alcohol Dehydrogenation over Au/Birnessite Photocatalyst, *Appl. Catal., A*, 2016, **521**, 149–153, DOI: 10.1016/j.apcata.2015.10.027.

64 S. Chakrabarti, B. K. Dutta and R. Apak, Active Manganese Oxide: A Novel Adsorbent for Treatment of Wastewater Containing Azo Dye, *Water Sci. Technol.*, 2009, **60**(12), 3017–3024, DOI: 10.2166/wst.2009.758.

65 M. A. Cheney, P. K. Bhowmik, S. Qian, S. W. Joo, W. Hou and J. M. Okoh, A New Method of Synthesizing Black Birnessite Nanoparticles: From Brown to Black Birnessite with Nanostructures, *J. Nanomater.*, 2008, **1**, 1–8, DOI: 10.1155/2008/763706.

66 Q. Feng, K. Yanagisawa and N. Yamasaki, Synthesis of Birnessite-Type Potassium Manganese Oxide, *J. Mater. Sci. Lett.*, 1997, **6**(3), 5–7, DOI: 10.1023/A:1018577523676.

67 A. I. Zaitsev, M. A. Zemchenko and B. M. Mogutnov, Thermodynamic Properties of Manganese Silicides, *Zh. Fiz. Khim.*, 1989, 1451–1458.

68 A. M. El-Sawy, C. K. King'ondu, C.-H. Kuo, D. A. Kriz, C. J. Guild, Y. Meng, S. J. Frueh, S. Dharmarathna, S. N. Ehrlich and S. L. Suib, X-Ray Absorption Spectroscopic Study of a Highly Thermally Stable Manganese Oxide Octahedral Molecular Sieve (OMS-2) with High Oxygen Reduction Reaction Activity, *Chem. Mater.*, 2014, **26**(19), 5752–5760, DOI: 10.1021/cm5028783.

69 K. T. Jacob, A. Kumar, G. Rajitha and Y. Waseda, Thermodynamic Data for Mn_3O_4, Mn_2O_3 and MnO_2, *High Temp. Mater. Processes*, 2011, **30**(4), 459–472, DOI: 10.1515/HTMP.2011.069.

70 W. Y. Hernández, M. A. Centeno, S. Ivanova, P. Eloy, E. M. Gaigneaux and J. A. Odriozola, Cu-Modified Cryptomelane Oxide as Active Catalyst for CO Oxidation Reactions, *Appl. Catal., B*, 2012, **123–124**, 27–35, DOI: 10.1016/j.apcatb.2012.04.024.

71 C. González, J. I. Gutiérrez, J. R. González-Velasco, A. Cid, A. Arranz and J. F. Arranz, Application of Differential Scanning Calorimetry to the Reduction of Several Manganese Oxides, *J. Therm. Anal. Calorim.*, 1998, 985–989, DOI: 10.1023/A:1010132606114.

72 Q. Xue and Q. Zhang, Agar Hydrogel Template Synthesis of Mn_3O_4 Nanoparticles through an Ion Diffusion Method Controlled by Ion Exchange Membrane and Electrochemical Performance, *Nanomaterials*, 2019, **9**(4), 503, DOI: 10.3390/nano9040503.

73 K. Stangeland, D. Y. Kalai, Y. Ding and Z. Yu, Mesoporous Manganese-Cobalt Oxide Spinel Catalysts for CO_2 Hydrogenation to Methanol, *J. CO_2 Util.*, 2019, **32**(January), 146–154, DOI: 10.1016/j.jcou.2019.04.018.

74 A. Sápi, G. Halasi, A. Grósz, J. Kiss, A. Kéri, G. Ballai, G. Galbács, Á. Kukovecz and Z. Kónya, Designed Pt Promoted 3D Mesoporous Co_3O_4 Catalyst in CO_2 Hydrogenation, *J. Nanosci. Nanotechnol.*, 2018, **19**(1), 436–441, DOI: 10.1166/jnn.2019.15779.

75 S. Kattel, P. Liu and J. G. Chen, Tuning Selectivity of CO_2 Hydrogenation Reactions at the Metal/Oxide Interface, *J. Am. Chem. Soc.*, 2017, **139**(29), 9739–9754, DOI: 10.1021/jacs.7b05362.

76 Q. Liu, Y. Han, J. Cai, E. J. Crumlin, Y. Li and Z. Liu, CO_2 Activation on Cobalt Surface in the Presence of – H_2O: An Ambient-Pressure X-Ray Photoelectron Spectroscopy Study, *Catal. Lett.*, 2018, **148**(6), 1686–1691, DOI: 10.1007/s10562-018-2362-z.

77 D. R. J. Kolling, N. Cox, G. M. Ananyev, R. J. Pace and G. C. Dismukes, What Are the Oxidation States of Manganese Required To Catalyze Photosynthetic Water Oxidation?, *Biophys. J.*, 2012, **103**, 313–322, DOI: 10.1016/j.bpj.2012.05.031.

78 G. Varga, A. Sápi, T. Varga, K. Baán, I. Szenti, G. Halasi, R. Mucsi, L. Óvári, J. Kiss and Z. Fogarassy, *et al.*, Ambient Pressure CO_2 Hydrogenation over a Cobalt/Manganese-Oxide Nanostructured Interface: A Combined *in Situ* and *Ex Situ* Study, *J. Catal.*, 2020, **386**, 70–80, DOI: 10.1016/j.jcat.2020.03.028.

79 J. Gómez-Pérez, D. G. Dobó, K. L. Juhász, A. Sápi, H. Haspel, Á. Kukovecz and Z. Kónya, Photoelectrical Response of

This journal is © the Owner Societies 2020

Phys. Chem. Chem. Phys., 2020, **22**, 13999–14012 | **14011**

Mesoporous Nickel Oxide Decorated with Size Controlled Platinum Nanoparticles under Argon and Oxygen Gas, *Catal. Today*, 2017, **284**, 37–43, DOI: 10.1016/j.cattod.2016.10.026.

80 H. Wang, K. An, A. Sapi, F. Liu and G. A. Somorjai, Effects of Nanoparticle Size and Metal/Support Interactions in Pt-Catalyzed Methanol Oxidation Reactions in Gas and Liquid Phases, *Catal. Lett.*, 2014, **144**(11), 1930–1938, DOI: 10.1007/s10562-014-1347-9.

81 M. D. Porosoff, X. Yang, J. A. Boscoboinik and J. G. Chen, Molybdenum Carbide as Alternative Catalysts to Precious Metals for Highly Selective Reduction of CO_2 to CO, *Angew. Chem., Int. Ed.*, 2014, **53**(26), 6705–6709, DOI: 10.1002/anie.201404109.

82 R. W. Dorner, D. R. Hardy, F. W. Williams and H. D. K. Willauer, Mn Doped Iron-Based CO_2 Hydrogenation Catalysts: Detection of $KAlH_4$ as Part of the Catalyst's Active Phase, *Appl. Catal., A*, 2010, **373**(1–2), 112–121, DOI: 10.1016/j.apcata.2009.11.005.

83 H. Zhan, F. Li, C. Xin, N. Zhao, F. Xiao, W. Wei and Y. Sun, Performance of the La–Mn–Zn–Cu–O Based Perovskite Precursors for Methanol Synthesis from CO_2 Hydrogenation, *Catal. Lett.*, 2015, **145**(5), 1177–1185, DOI: 10.1007/s10562-015-1513-8.

84 B. Liang, T. Sun, J. Ma, H. Duan, L. Li, X. Yang, Y. Zhang, X. Su, Y. Huang and T. Zhang, Mn Decorated Na/Fe Catalysts for CO_2 Hydrogenation to Light Olefins, *Catal. Sci. Technol.*, 2019, **9**(2), 456–464, DOI: 10.1039/c8cy02275e.

85 S. S. Kim, K. H. Park and S. C. Hong, A Study of the Selectivity of the Reverse Water-Gas-Shift Reaction over Pt/TiO_2 Catalysts, *Fuel Process. Technol.*, 2013, **108**, 47–54, DOI: 10.1016/j.fuproc.2012.04.003.

86 R. E. Owen, D. Mattia, P. Plucinski and M. D. Jones, Kinetics of CO_2 Hydrogenation to Hydrocarbons over Iron–Silica Catalysts, *ChemPhysChem*, 2017, **18**(22), 3211–3218, DOI: 10.1002/cphc.201700422.

87 Z. J. Liu, X. J. Tang, S. Xu and X. L. Wang, Synthesis and Catalytic Performance of Graphene Modified CuO–ZnO–Al_2O_3 for CO_2 Hydrogenation to Methanol, *J. Nanomater.*, 2014, 690514, DOI: 10.1155/2014/690514.

88 P. A. U. Aldana, F. Ocampo, K. Kobl, B. Louis, F. Thibault-Starzyk, M. Daturi, P. Bazin, S. Thomas and A. C. Roger, Catalytic CO_2 Valorization into CH_4 on Ni-Based Ceria-Zirconia. Reaction Mechanism by Operando IR Spectroscopy, *Catal. Today*, 2013, **215**, 201–207, DOI: 10.1016/j.cattod.2013.02.019.

14012 | *Phys. Chem. Chem. Phys.*, 2020, **22**, 13999–14012

This journal is © the Owner Societies 2020